AIChE WILEY InterScience® DISCOVER SOMETHING GREAT

Measurements and CFD Simulations of Gas Holdup and Liquid Velocity in Novel Aircraft Membrane Contactor

Babak Jajuee, Argyrios Margaritis, Dimitre Karamanev, and Maurice A. Bergougnou
Dept. of Chemical and Biochemical Engineering, Faculty of Engineering, University of Western Ontario,
London, Ontario, Canada, N6A 5B9

S. A. Mohsen Karimian
Dept. of Mechanical and Materials Engineering, Faculty of Engineering, University of Western Ontario,
London, Ontario, Canada, N6A 5B9

DOI 10.1002/aic.11010

Liquid velocity and gas holdup were measured in a 690L pilot-scale rectangular airlift contactor, divided into aerated and nonaerated sections by two vertical rectangular polyester textile membranes. Horizontal flow through the porous membranes complicates flow fields to such an extent that conventional models cannot predict thoroughly velocity profile in the contactor. Experimental data obtained from laser doppler velocimetry (LDV) method were compared with numerical finite volume method (FVM), in order to determine the velocity profile in the downcomer zone of the contactor. In formulating the data, a realistic set of boundary conditions was implemented in the numerical method, resulted in satisfactory agreement between theory and experiment. The effects of the distance between the rectangular membranes and air bubble size on the velocity profile were also studied. © 2006 American Institute of Chemical Engineers *AIChE J,* 52: 4079–4089, 2006

Keywords: membrane bioreactor, velocity profile, airlift contactor, mixing, hydrodynamics, multi-phase flow, biochemical engineering, bubble phenomena, computational fluid dynamics (CFD), fluidization

Introduction

Owing to the potential for complete mineralization and lower cost, airlift contactors (ALC) are widely used as an emerging technology for wastewater treatment and other three-phase applications.[1,2,3,4,5,6] There is an overwhelming supply of configurations and modifications of ALCs, mainly for expeditious biodegradation of environmental pollutants. Nonetheless, one has many hurdles to overcome in design and scaleup (or down) of ALCs since the fluid dynamics of these pneumatic vessels are often difficult to model. Most authors[7,8,9,10,11] have tried to model liquid-velocity profile, using hydrodynamic parameters, such as ε_g, U_{sg}, D, L, and so on, without getting into difficulties of solving Navier-Stokes equations, based on momentum transport. Previous theoretical developments might be regarded useful for studying ALCs with simple flow patterns. However, satisfactory agreement between theory and experiment is not attainable when the structure of the flow is complex or when geometry of ALCs changes.[12] It is of value, therefore, to supersede the conventional models with a self-reliant numerical model, based on mechanism of momentum transport and combine it with a precise measuring method in order to determine the velocity profile in ALCs with complex flow structure.

A new airlift contactor system, known as immobilized soil bioreactor system (ISBR), was developed for bioremediation of water-soluble recalcitrant pollutants[13] and bioleaching of gold ores.[14] Cell immobilization has added advantages compared to suspended microbial cultures, such as higher-biomass concentration, higher-metabolic activity, greater resistance to toxicity, better sludge properties, and so on.[15,16,17,18,19] In addition to these advantages, ISBR has a unique, but complex velocity profile that increases the rate of mass transfer and

---

Correspondence concerning this article should be addressed to A. Margaritis at amarg@uwo.ca.

decreases mixing time to the same order of CSTR reactors. The rigid membrane that separates the riser from the downcomer in conventional ALCs has been replaced with a semipermeable textile membrane in the ISBR, which is permeable to liquid and nonpermeable to gas bubbles. As a result, both vertical and horizontal flows are generated in these zones without exerting high-shear stress encountered in CSTR systems by impellers. In other words, aeration of one side of the porous medium exploits hydrostatic pressure differences, and runs liquid upwardly in the gassed section, downwardly in the ungassed section, and horizontally through the tortuous paths across the porous textile membrane from the unaerated to aerated zone.[12] The horizontal flow not only has a pronounced effect on mass-transfer rate, but also is responsible for attaching microorganisms to the textile membrane (soil immobilization), providing nutrients and oxygen for immobilized microorganisms. Due to the forgoing properties, the ISBR shows great improvement in biotreatment of persistent pollutants dissolved in water. Diffusion and convection into the interyarn and intrayarn pores of the textile membrane associated with fluid circulation in a defined cyclic pattern are the dominant mechanisms of mass and momentum transport. Microbial growth rate depends on hydrodynamic characteristics and transport of nutrients, oxygen, and contaminants, which in turn are governed by velocity profiles in the vicinity of textile media.

This work aims at applying both experimental and numerical methods of laser doppler velocimetry (LDV) and finite volume method (FVM), respectively, to analyze fluid trajectories across the porous textile membranes. Although more accurate models are required to capture the details of the flow field, such as turbulent fluctuations, the simple CFD model used here could adequately simulate the time-averaged features of the flow field, including the effect of the convection on the penetrating flow into the porous membrane. The results are of paramount importance in enhancing the efficiency of the ISBR and scaling up the bioreactor system for industrial purposes. It should be remarked that in the disciplinary jargon of this article the term convection connotes convective flow that is detectable by the LDV method.

Experimental

Apparatus

Figure 1 shows the airlift contactor and LDV system used to measure fluid velocities. An argon-ion laser, a probe, a beam separator, a signal processor, and a computer comprised the LDV components. The experiments were carried out in a rectangular tank, made of transparent plexiglass, with a working volume of 690L, dimensions of 76 cm × 76 cm × 119 cm, and wall thickness of 2 cm, as shown in Figure 2. The tank was divided up into aerated and nonaerated zones using two rectangular pliable sheets of nonwoven polyester textile membranes. Each membrane was supported with two stainless steel mesh of 5 cm opening size and 3 mm wire dia. The width and length of the membranes were 72 cm and 96 cm, respectively, suitable enough to be fixed inside the tank. The thickness of each textile membrane was 1 cm, and its porosity was 0.995, as illustrated in Figure 3. Water permeability is the measure of the ease of water flow through a porous membrane, commonly referred to as hydraulic conductivity. Permittivity is permeability divided by the thickness of the layer through which flow occurs, see Eqs. 15–17. The Permittivity of the textile membrane was 1.7 s^{-1}. Liquid height above the membrane (top clearance), and under it (bottom clearance) was both kept constant at 10 cm. Air was distributed using a flexible rubber porous air tube (Marineland, USA), which was equipped with ceramic weights to be held in place, and cleaning ring to be slid along the tube to prevent clogging. The large surface area of the air tube required very little pressure to provide diffused aeration and stock the riser with air bubbles. Small-sized air bubbles of 3mm were formed uniformly at the sparger, from which they broke off and rose at an average velocity of 0.3 m/s through the liquid. To study the effect of sparger on velocity profile in the contactor system, the flexible air tube was replaced with a rigid stainless steel one, having 50 holes with diameter of 0.5 mm each. The average bubble size produced by this sparger was about 1.5 cm.

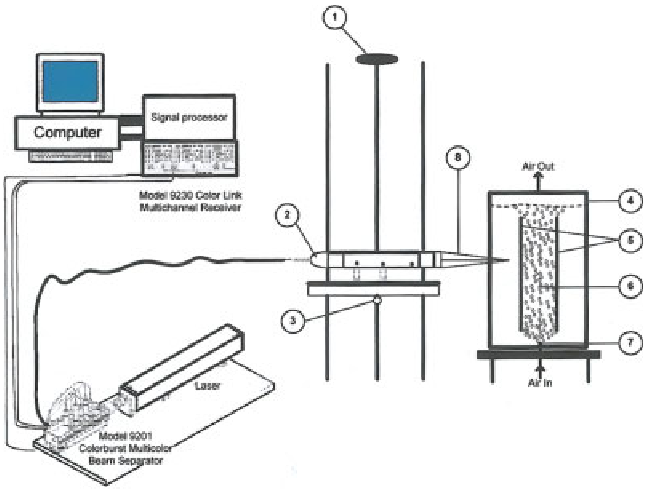

Figure 1. Experimental setup for LDV system and airlift contactor: (1) vertical lead screw gear, (2) 6-beam probe model 9833, (3) horizontal lead screw gear, (4) airlift contactor, (5) porous textile membrane, (6) gas bubbles, (7) flexible rubber tube air sparger, and (8) laser beams.

[Color figure can be viewed on the online issue, which is available at www.interscience.wiley.com.]

Gas holdup

The overall gas holdup was calculated at each superficial gas velocity, using Eq. 1

$$\frac{\varepsilon_g = \Delta H}{(\Delta H + H_L)} \tag{1}$$

where H_L and ΔH represent the ungassed liquid height and the increase in liquid level after gassing, respectively.

Local holdup was also obtained along the riser from the axial pressure difference measured by eight pressure probes mounted at 0, 20, 40, 60, 80, 100, and 110 cm from the column bottom, using Eq. 2

$$\varepsilon_g = 1 - \frac{\Delta P}{\rho g \Delta H} \tag{2}$$

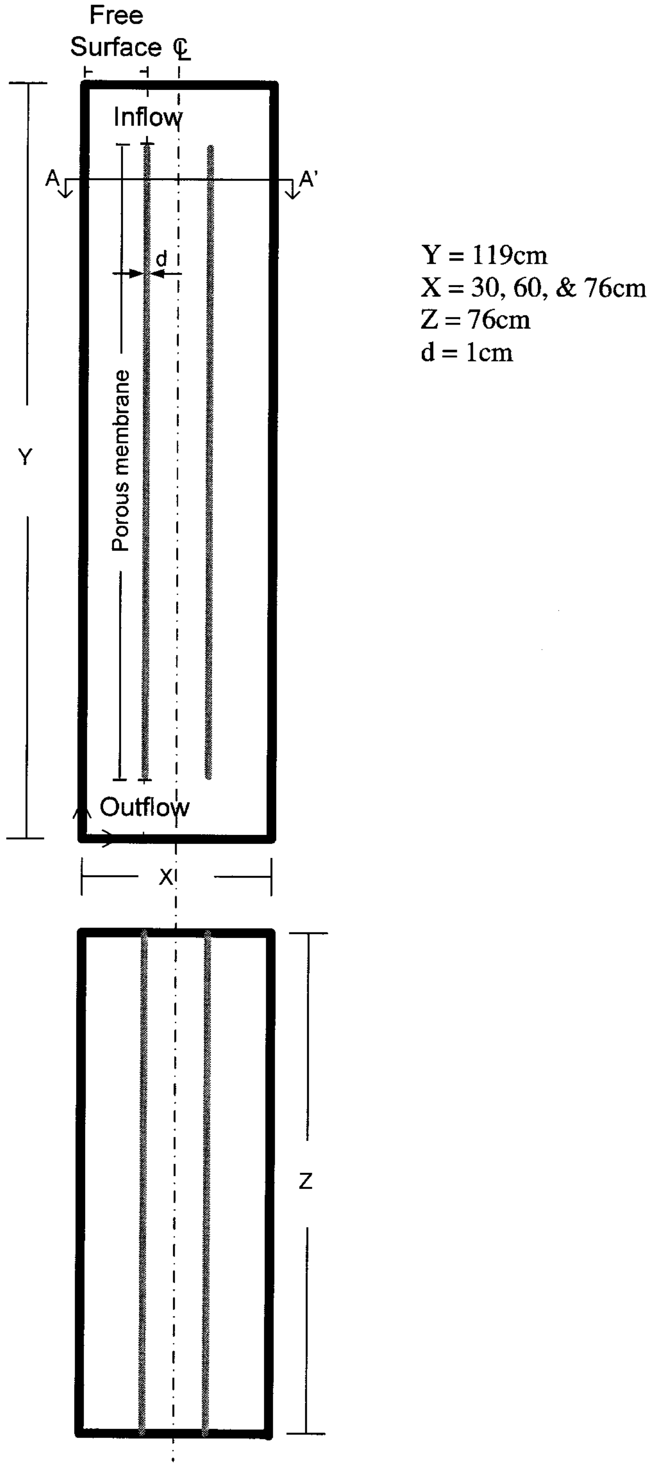

Figure 2. Geometry of rectangular airlift contactor.

where ρ is the liquid density. Holdup values from the above techniques have been compared in Figure 4.

Flow visualization

The flow was visualized with laser induced fluorescence (LIF) technique. The 488 nm (blue) line of a 4 W argon-ion laser was used to excite the fluorescence dye added to the airlift contactor at a constant rate. A cylindrical lens was applied to produce an approximately 3 mm thick laser sheet, which was oriented vertically, and normal to the porous textile membrane. Images formed from fluorescence emission were recorded digitally at a rate of 60 frames per s. A 500 nm high-pass light filter was used to suppress the excitation of blue light, thereby, allowing only the fluorescent light to be recorded, and reducing background light noise.

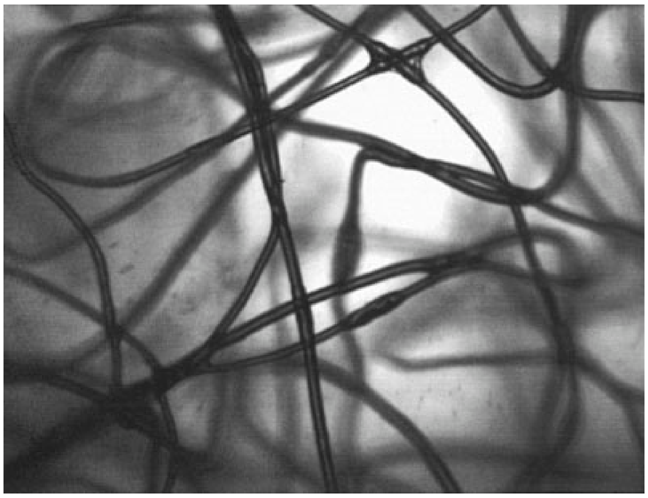

Figure 3. Polyester textile membrane fibers, 50 magnification, porosity 0.995, and permittivity 1.7 s^{-1}.

LDV Measurements

The measurements were carried out using a three-component laser doppler velocimetry system (TSI, Inc., USA) in backscatter mode. As illustrated in Figure 1, light from an argon-ion laser was separated by the colorburst into blue, green, and violet beams of 488 nm, 514 nm, and 476 nm wavelengths, respectively. The probe beam diameter was 1.8 mm. These transmitting beams

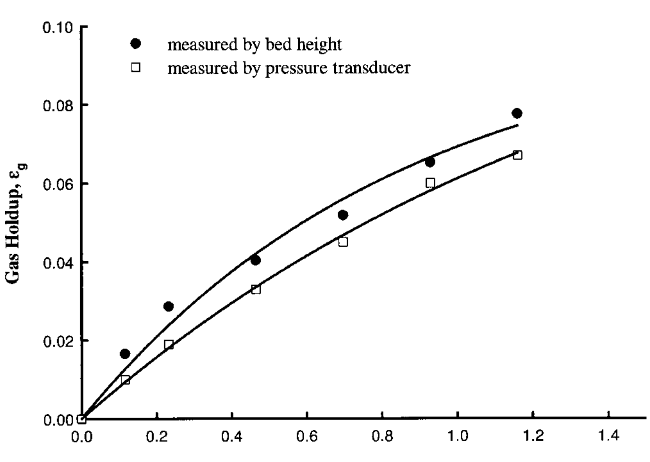

Figure 4. Comparison of gas holdup values measured by bed height and pressure-transducer methods.

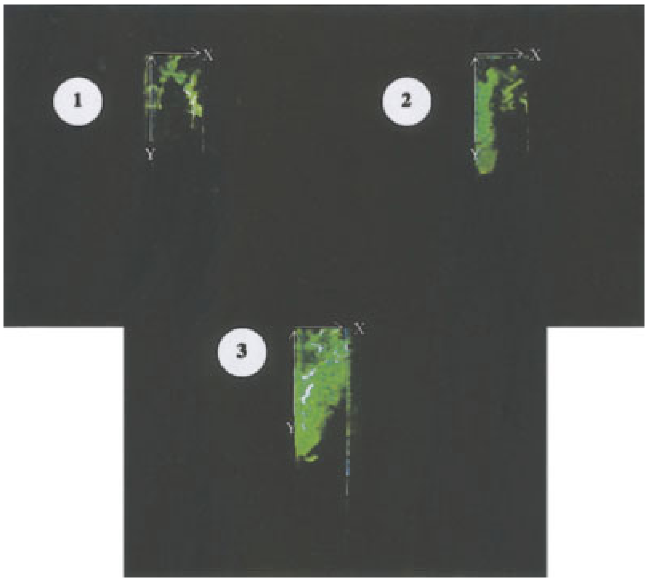

Figure 5. Flow pattern visualization with laser induced fluorescence (LIF) technique.

(1) injected dye under the entrance of downcomer toward the rigid wall, (2) wall jet moves down, and (3) a strayed part of the wall jet turns aside and clips the textile membrane, due to separation of vortex. [Color figure can be viewed on the online issue, which is available at www.interscience.wiley.com.]

were linked to the probe with 1041.40 mm length and 172.72 mm dia. through fibers that connected to the Model 9271 Fiber couplers on the colorburst. The transmitting lens whose diameter was 155 mm had a focal length (in air) of 757.7 mm, resulting in a measuring volume diameter and length of 0.115 mm and 2.7 mm, respectively. The scattered light from the particles was collected by the probe through a single, multimode receiving fiber that was connected to Colorlink. In the Colorlink, the light was separated by colors and converted to electrical signals. These signals were sent to a signal processor, which extracted frequency data from the signals. The data was then analyzed and displayed through the Find Software, using single measurement per burst (SMB) mode. A three-axis motor- driven traversing unit was used to move the LDV probe in all three directions by means of two vertical and horizontal lead screw gears, with a relative position accuracy (precession) of 0.015 mm per 100 mm of travel, and a minimum displacement of 0.0025 mm per step. Vertical and horizontal velocity profiles were measured exhaustively, carrying out five different runs at each probe position at one side of the tank. Velocity profile was built up in the downcomer over a matrix of in Y and X directions. In the Y direction the LDV probe was mounted at Y = 4.55, 13.75, 34.25, 59.75, 69.25, 90.75, 105.25, and 115.25 cm from the bottom of the tank. In the X direction, the measurements were carried out at three depths of X = 1, 5, and 9 cm that were close to the wall, at the center of the downcomer, and close to the membrane, respectively. The probe was symmetrical vs. the width of the membrane, Z = 38 cm, since there was no detectable flow in this direction. The horizontal and vertical velocities at each location of the matrix were measured at four different superficial-gas velocities of 0.023, 0.046, 0.092, and 0.138 cm/s. To do so, the flow was seeded using silicon carbide particles with an average dia. of 2 μm, density of 3.2 g/cc, and surface area of 9–11 m^2/g. These particles were added to increase the effective data rate by roughly a factor of 10.

Numerical Model

A three-dimensional (3-D) parallel Navier-Stokes solver, ParTISUN,[20] was employed to model numerically the flow inside the downcomer. The Navier-Stokes solver implements a finite-volume method (FVM) to solve the integral form of the conservation equations for laminar mass and momentum transfer. The main purpose of using the numerical simulations was to evaluate the ability of a simple CFD tool in predicting the overall features of the flow, mostly the average velocity profile. Accordingly, a simple large eddy simulation "LES" model was implemented in the code to simulate "very" large eddies and model the filtered turbulent structures. The level of accuracy of the LES model is selected so that it can predict the average features of the flow field. All simulations were performed in three dimensions and in actual scale of the airlift contactor system with the bulk properties of water. A segment

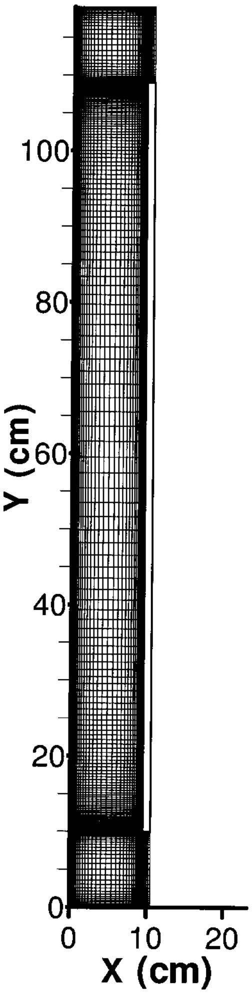

Figure 6. Grid generated by FVM discretizes the downcomer zone and contains cells in the X, Y, and Z directions, respectively.

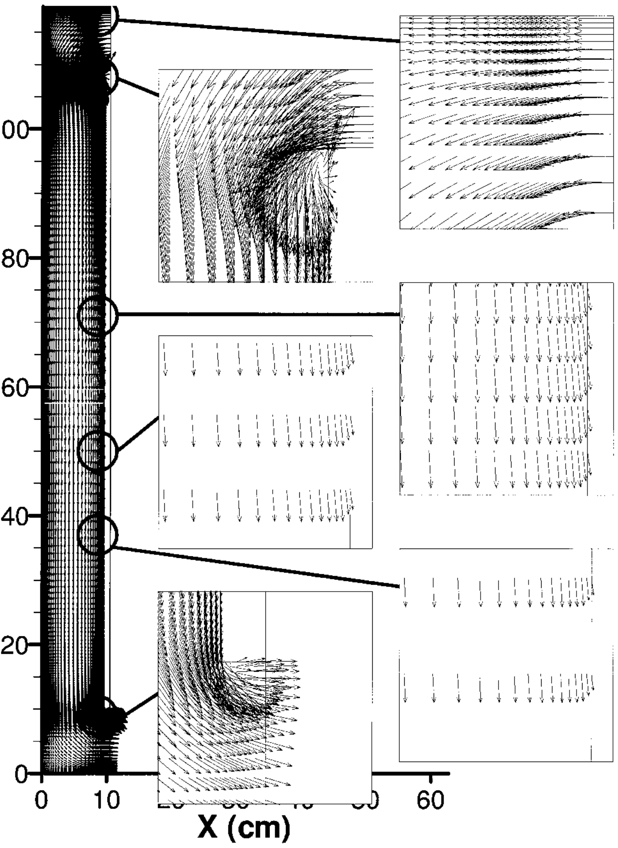

Figure 7. Partial magnification of velocity vectors predicted by FVM in the downcomer: vertical velocity vectors weaken along the rigid wall, and so do both vertical and horizontal vectors along the membrane.

Velocity vectors increase close to the exit where the stream makes a sudden turn and accelerates in the X direction.

of the downcomer with 10 cm depth in Z direction is selected as the computational domain.

Governing equations

For an arbitrary fixed control volume ΩCR^3, of volume V and a piecewise smooth boundary 2Ω, with unit normal vector n_i pointing outwards, occupied by continuum, the governing equations for the incompressible flow, ρ constant, are

$$\int_{\partial\Omega} \rho u_j n_j \mathrm{d}S = 0, \tag{3}$$

$$\int_{\Omega} \rho u_{i,j} \mathrm{d}V + \int_{\partial\Omega} n_j(\rho u_j u_i - \mu u_{i,j}) \mathrm{d}S = -\int_{\partial\Omega} P n_i \mathrm{d}S + \int_{\Omega} S_i^T \mathrm{d}V, \tag{4}$$

where u_t is the velocity vector, $\mathrm{d}S$ is the surface differential, $\mathrm{d}V$ is the volume differential, and S_i^T is the turbulent source term. The turbulent source term in Eq. 4 is defined as follows

$$S_i^T = 2(\mu_t \, \overline{S}_{ij}),j, \tag{5}$$

where μ_t is the turbulent viscosity and

$$\overline{S}_{ij} = \frac{1}{2}(u_{i,j} + u_{j,i}). \tag{6}$$

The basic LES method developed by Smagorinsky[21] was used to determine the turbulent viscosity

$$\mu_t = \rho(C_S\overline{\Delta})^2|\overline{S}|, \tag{7}$$

in which

$$C_S = 0.01, \quad \overline{\Delta} = (\mathrm{d}V)^{\frac{1}{3}}, \quad \text{and} \quad |\overline{S}| = (\overline{S}_{ij}\overline{S}_{ij})^{\frac{1}{2}}. \tag{8}$$

Boundary conditions

The key to a robust and accurate simulation is finding a suitable and simplified set of boundary conditions. Figure 2 shows a 2-D view of the downcomer zone. Since the majority of the flow at the inlet of the downcomer is horizontal toward

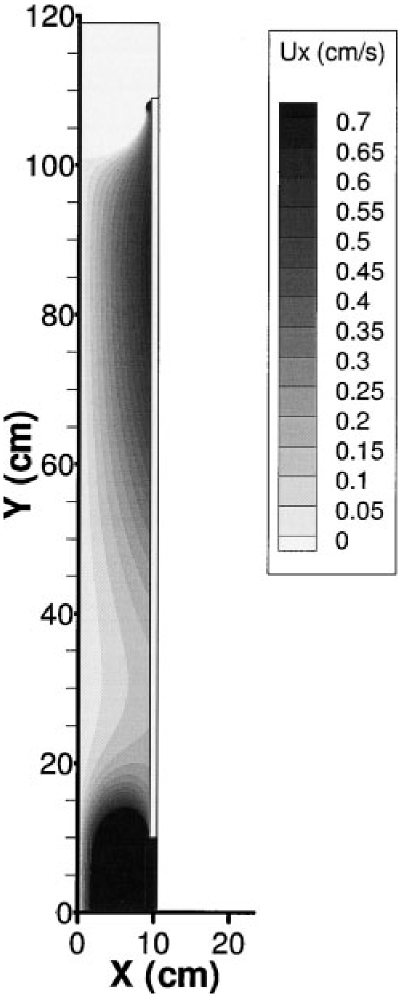

Figure 8. Horizontal velocity contour in downcomer: light area at the top of the downcomer is due to the negative horizontal flows.

Lighter areas show lower magnitude of horizontal flow along downcomer.

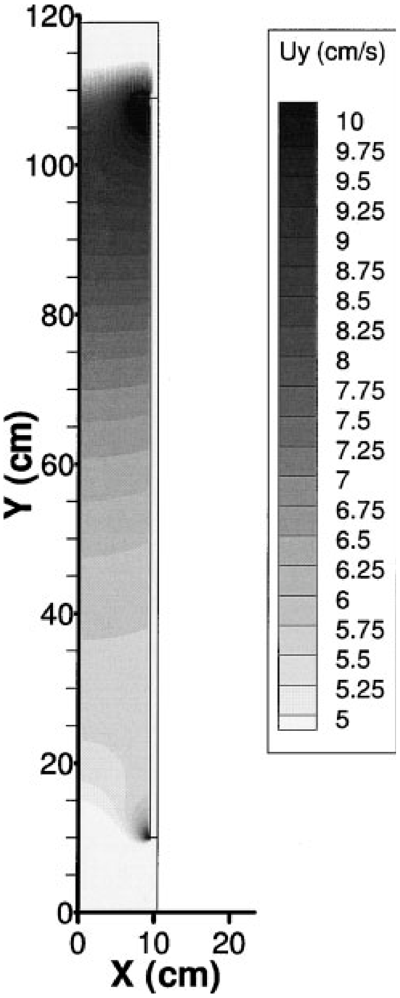

Figure 9. Vertical velocity contour: part of surface jet converges to vertical wall jet and surges down, and loses its intensity along the downcomer.

Arrows show the direction of flow.

the rigid wall of the airlift contactor, a bulk inflow boundary condition was imposed at this region

$$U_x = -u_{in}, \qquad U_y = 0, \qquad U_z = 0. \tag{9}$$

hence, the free surface at this region was characterized by a no-shear boundary condition

$$\frac{\partial U_x}{\partial y} = 0, \qquad U_y = 0, \qquad \frac{\partial U_z}{\partial y} = 0. \tag{10}$$

It is plausible to assume a steady-flow field within the timescale of our interest. Hence, a zero gradient outflow boundary condition is imposed at the outlet of the downcomer

$$\frac{\partial U_x}{\partial n_b} = 0, \qquad \frac{\partial U_y}{\partial n_b} = 0, \qquad \frac{\partial U_z}{\partial n_b} = 0. \tag{11}$$

in which n_b is the normal vector of the boundary face. A no-slip boundary condition was applied at the walls

$$U_x = U_y = U_z = 0. \tag{12}$$

There are two choices of periodic and symmetry boundary conditions that either can represent the flow behavior at the walls normal to the Z direction. A symmetry-boundary condition was applied at the walls normal to the Z direction

$$\frac{\partial U_x}{\partial z} = 0, \qquad \frac{\partial U_y}{\partial z} = 0, \qquad U_z = 0. \tag{13}$$

As a closure to the continuity equation, a constant relative pressure was imposed at the outlet

$$P_{\text{outlet}} = 0 \tag{14}$$

whereby, the pressure in any place along the downcomer could be extrapolated from the flow field to the boundaries of the domain. The boundary condition at the porous membrane should represent bulk-flow resistance in an isotropic porous medium. This was accomplished by using Darcy's law[22] which is a phenomologically derived constitutive equation, describing the flow of a fluid through a porous medium (typically water through an aquifer). Darcy's law states that the

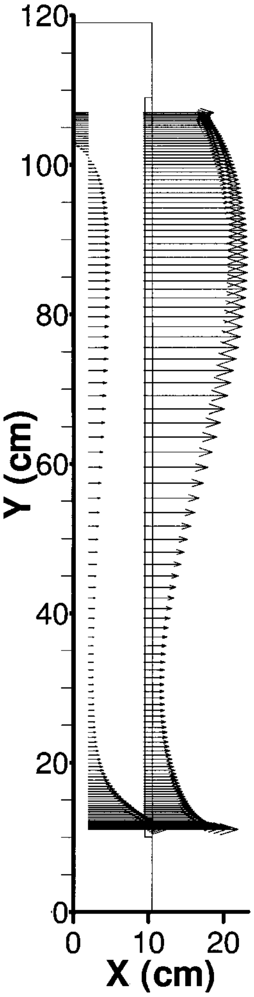

Figure 10. Horizontal velocity profiles on the porous textile membrane and on a cross section at X = 1.5 cm.

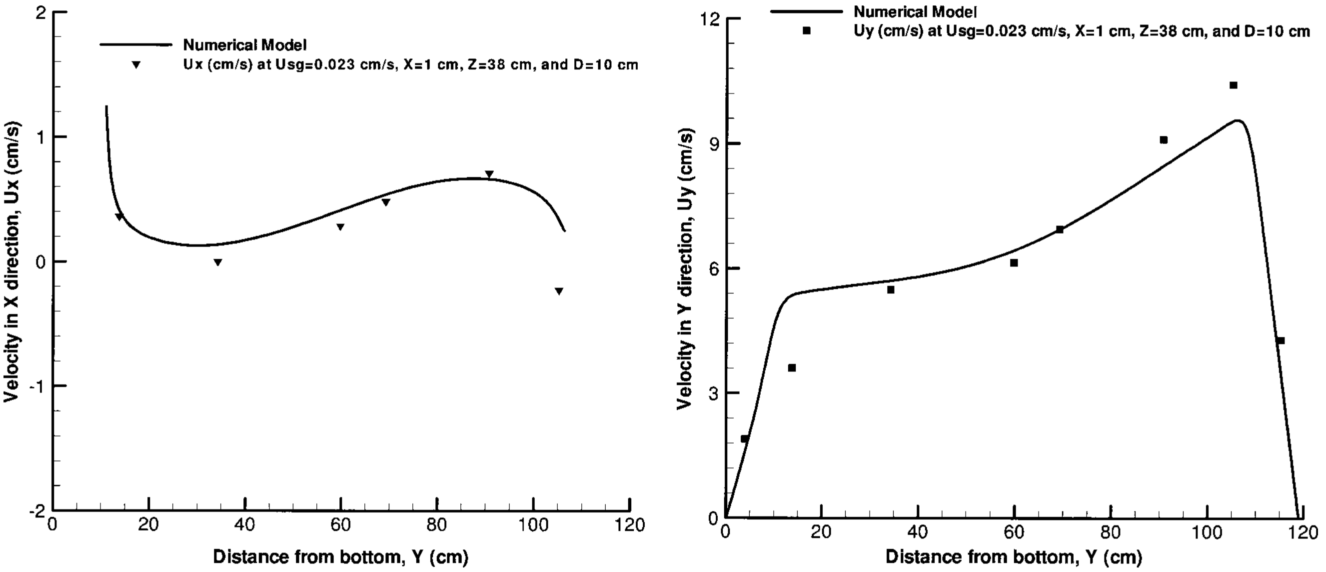

Figure 11. (a) X-directed velocities vs downcomer height Y at X = 1 cm, and Z < 38 cm, and (b) Y-directed velocities vs downcomer height Y at X = 1 cm, and Z = 38 cm.

The solid lines are predicted by the numerical model.

rate of fluid flow through a porous membrane is proportional to the potential energy gradient within that fluid

$$-\frac{\partial P}{\partial x} = (\mu/K)u_{pb}, \qquad (15)$$

where P is the fluid pressure at the membrane surface in the downcomer zone, K is permeability coefficient and u_{pb} is the infiltrated-fluid velocity. The constant of proportionality is the hydraulic conductivity; which in turn is a property of both the porous membrane, and the fluid moving through the membrane. The permittivity of the textile membrane is defined (ASTM 1992)

$$\psi = \left(\frac{\rho g}{\mu}\right)\frac{K}{d} \qquad (16)$$

where is d the textile thickness. The driving force caused by hydrostatic pressure differences between the riser and downcomer depends on gas holdup in the riser. Gas holdup in the riser and relative pressure of the fluid were measured to determine the size of pressure gradient. At any given height in the fluid y, the pressure gradient in the membrane is (see Figure 2)

$$\frac{\partial P}{\partial x} = \frac{\rho g(119-y)(1-\varepsilon_g) - [P+\rho g(119-y)]}{d} = -\frac{P+\rho g(119-y)\varepsilon_g}{d}, \qquad (17)$$

Therefore, the boundary condition at the porous wall becomes

$$\frac{\mu u}{K} = \frac{P+\rho g(119-y)\varepsilon_g}{d}, \qquad U_y = 0, \qquad U_z = 0. \qquad (18)$$

For simplicity's sake, it is preferable to refer to gas holdup as a constant parameter along the riser. Therefore, spatial arrangement of bubbles formed at the orifice and that at top of the riser is assumed to be constant. Gas holdup was found to depend on superficial gas velocity at fixed orifice diameter. Godbole et al.[23] proposed the following correlation for gas holdup in Newtonian solutions

$$\varepsilon_g = 0.255U_{sg}^{0.6}\mu^{-0.19} = \alpha U_{sg}^{\beta} \qquad (19)$$

where U_{sg} is superficial gas velocity and μ is liquid viscosity. Larger bubbles have shorter residence time and higher-terminal velocity. Therefore, larger orifice diameters reduce holdup at fixed gas flow rate. As the orifice diameter increases from 0.5 to 3 mm, exponent β in Eq. 19 decreases[24] in water from 1 to 0.79 and constant α from 2.8 to 0.76.

Results and Discussion

Air bubbles form at the flexible porous air tube, from which they break off and rise through the liquid, bursting finally at the liquid surface. The liquid, driven upward along the riser, enters the downcomer as a surface jet. This surface jet impacts the rigid wall of the contactor and induces simultaneously two major flow streams. One is a wall jet whose strength is attenuated by degrees when surging down. Both shear forces, as well as subtraction of the horizontal flow into the membrane weaken the strength of the wall jet at downstream areas. Another flow is the one that rebounds from the wall and pounds the porous membrane. This stream is perforce responsible for the majority of horizontal flow and spinning vortexes at the top of the textile membrane. A useful synopsis of the mean flow field of surface jets has been reviewed.[25] The flow visualization technique shows the behavior of the surface jet in vicinity of the wall and the porous membrane, as illustrated in Figure 5. It can be seen that the injected dye under the entrance of downcomer rushes toward the rigid wall and surges down, while a strayed part of it turns aside and clips the textile membrane. In essence, the Reynolds number at the surface

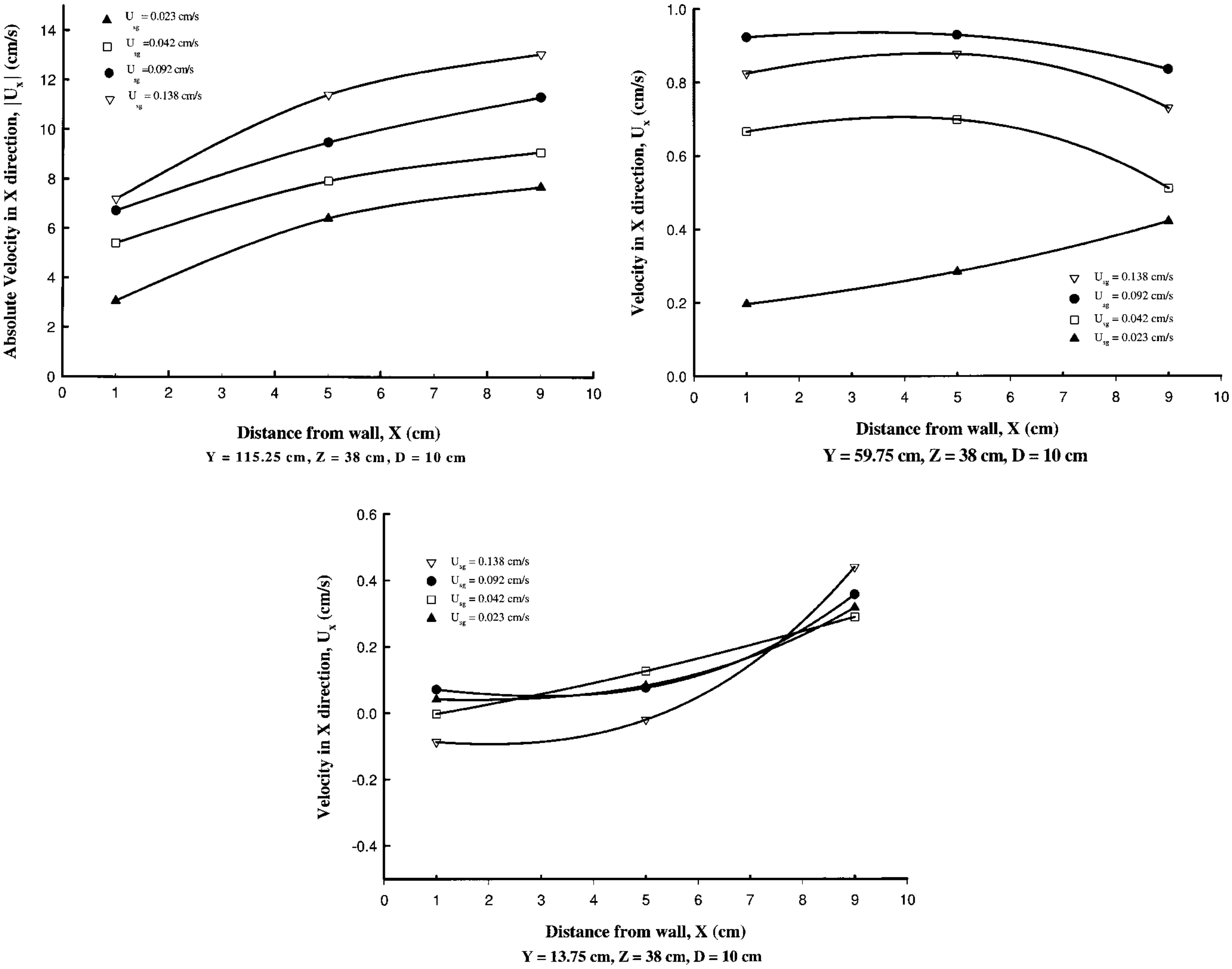

Figure 12. (a), (b), and (c): Comparison of horizontal velocity magnitudes at three distances from the wall in the X direction.

jet depends on both superficial-gas velocity and size of gas bubbles. Small bubbles provide higher specific surface area and propel higher volume of liquid upward when rising through the liquid. Therefore, the riser which is abounding in myriads of small bubbles provides higher Reynolds number at the entrance of the downcomer. Even though Eq. 15 suggests that higher hydrostatic-pressure difference should produce more horizontal flow at the bottom of the downcomer, the strength of the surface jet outweighs the effect of hydrostatic-pressure difference in the downcomer. Flow field in the downcomer was numerically simulated for the case of $U_{sg} = 0.023$ cm/s. A grid of 36 × 210 × 36 with a wall grid size of $\Delta_w/W = 5 \times 10^{-3}$ and a biexponential grid expansion in the X direction was generated to discretize the computational domain. The biexponential coefficient was 0.86. Figure 6 shows a 2-D view of the grid in the X-Y plane. A nondimensional time-step of $\Delta t^* = (u_{in}/W)\Delta t = 0.1$ was selected. To reach a quasi-steady flow, the simulation was performed for a period of eight flow-through times, which is equivalent to $t^* = 96$ or 960 time-steps. The results for the last three flow-through times were averaged. Since the experimental measurement were all taken in two dimensions in the X-Y plane at Z = 38 cm, all the numerical results are for the average quantities in the X-Y plane at the middle of the computational domain ($Z_{\text{comp}} = 5$ cm). The wall friction velocity was calculated as $u_\tau = \sqrt{\nu(\partial v/\partial x)_{wall}}$ and estimated as $u_\tau = 0.121$ cm/s as a result of the simulation. Consequently, there are three grid points within $y^+ \leq 5$, where y^+ is the wall coordinate and is defined as $y^+ = (u_\tau y)/\nu$. Therefore, the grid resolution near the wall is high enough to give a good estimation of the wall layer. Figure 6 shows that the grid density is higher in the regions with higher shear flows, that is, close to the wall, and where the flow is accelerating or decelerating. The intensity of the wall jet, and, thus, the velocity magnitude decrease as the fluid flows downstream. Figure 7 shows the velocity vectors predicted by FVM in the downcomer. The accelerating flow formed at the top of the downcomer is in a good agreement with what visualized in Figure 5. It is interpreted that, vertical velocity vectors weaken and slow down along the rigid wall and so do both vertical and horizontal vectors along the membrane. Velocity vectors increase close to the exit where the stream makes a sudden turn and accelerates in the X direction.

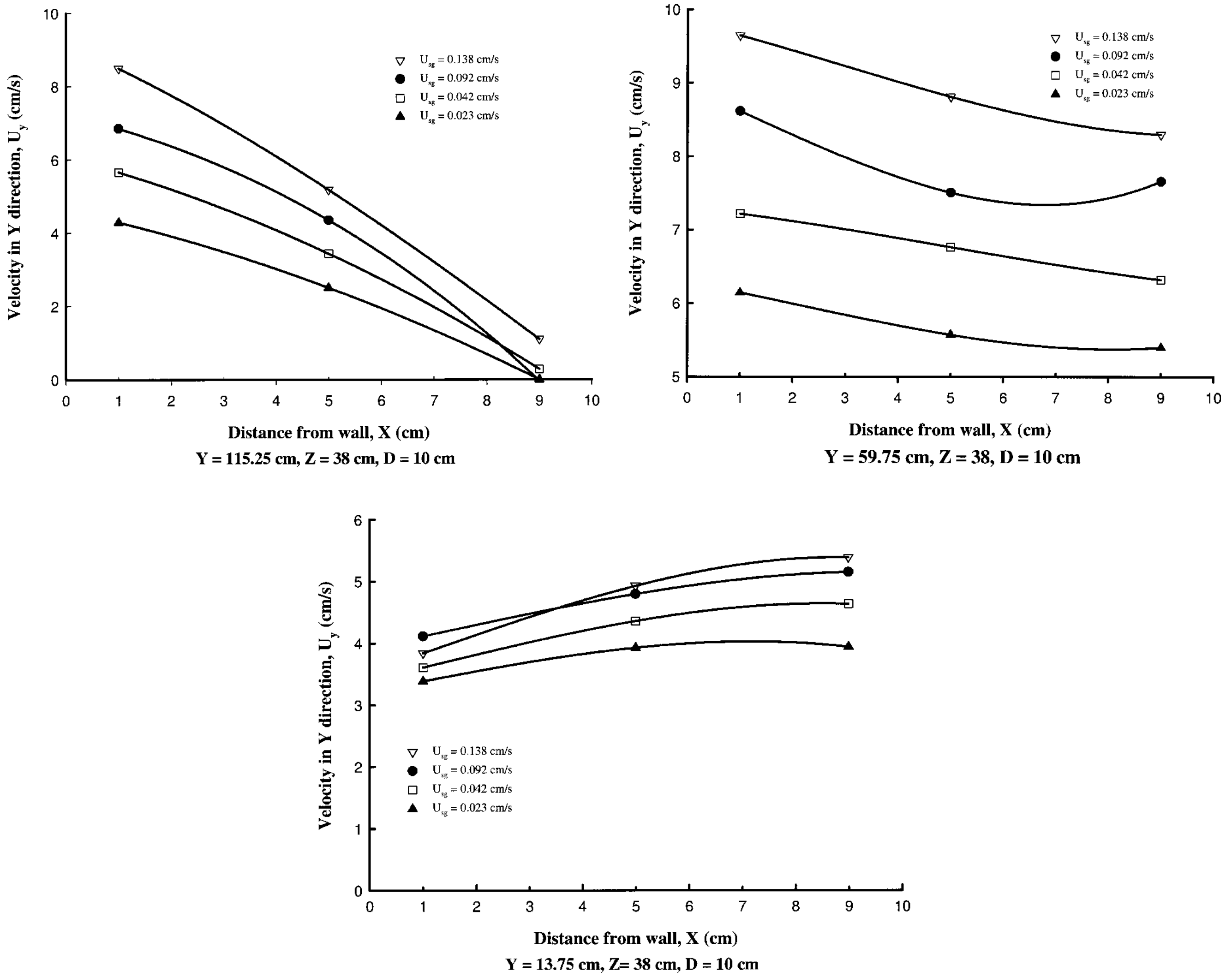

Figure 13. (a), (b), and (c): Comparison of vertical velocity magnitudes at three distances from the wall in the X direction.

It is evident that the wall jet and convection into the membrane decelerate downstream. Figure 8 shows the horizontal velocity contour in the downcomer. The light area at the top of the downcomer is due to the negative horizontal flows in this zone. Along the downcomer, the lighter areas pertain to lower magnitude of horizontal flow. Vertical velocity contour has been shown in Figure 9. The contour shows that there is almost no vertical velocity at the inlet and outlet regions where the flows are largely horizontal. In the region right below the inlet, however, the part of the horizontal surface jet that converts to the vertical wall jet surges down, and loses its intensity along the downcomer. The horizontal velocity profiles on the membrane and on a cross section at X = 1.5 cm has been depicted in Figure 10. It shows that the effect of surface jet is superimposed to the local effect of hydrostatic-pressure difference at the top of the membrane, where there is outflow from the downcomer to the riser. At the bottom of the membrane, 20 cm < Y < 40 cm, in which the effect of the surface jet has been diminished, the horizontal flow is mainly generated by the hydrostatic pressure differences. Based on Eq. 17, the hydrostatic-pressure difference has its highest amount in the bottom zone; nevertheless, the horizontal flow due to solely pressure difference cannot be detected by LDV method even at its maximum amount. In other words, the small horizontal flows at this region are located on LDV error domain, which is estimated as equal to zero. Accordingly, the nondetectable flow caused by hydrostatic pressure might be recognized as diffusion and/or penetration rather than convection into the membrane. The deceleration along the downcomer followed by acceleration near the outlet is noticeable in this profile.

Figure 11 illustrates the extent to which FVM correlates the LDV experimental data, in which X- and Y-directed experimental velocities along the downcomer have been shown at, U_{sg} = 0.023 cm/s X = 1 cm (close to the wall), and Z = 38 cm at the middle of the downcomer in the Z direction. At Y = 105.25 cm, flow is still a part of the surface jet, which is surging toward the rigid wall, and pointing in the opposite direction of X-axis. At Y = 90.75 cm the rebounded stream (horizontal flow) is in its maximum amount and heads toward the membrane. Horizontal and vertical flows decrease along the downcomer, while merely horizontal flow increases once again when the liquid squirts out of the exit. At other X-directed

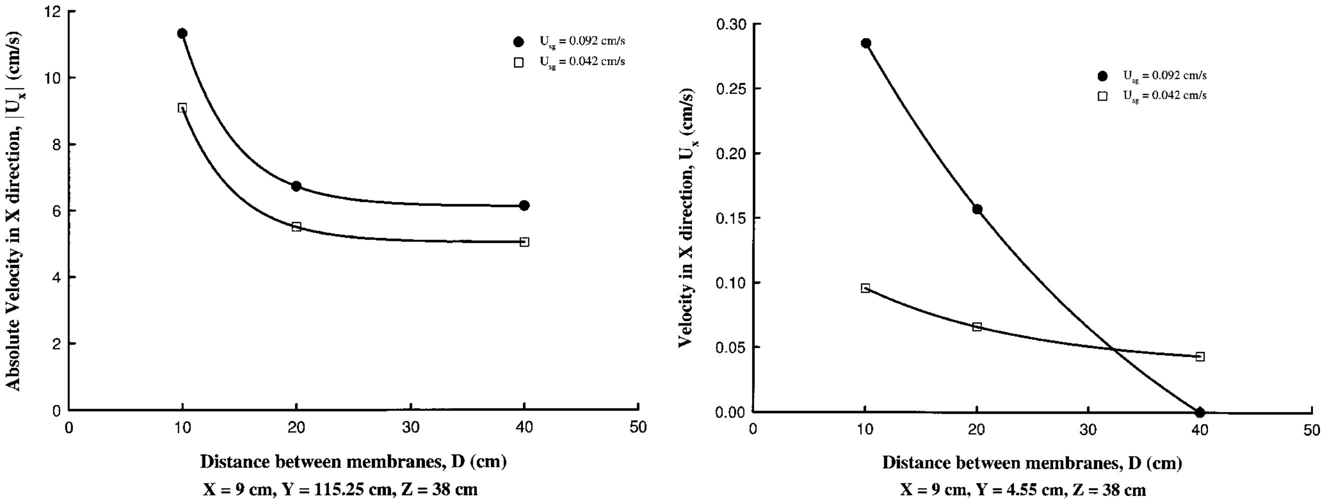

Figure 14. (a) Absolute value velocity in the X direction at Y = 115.25 cm as a function of distance between the two textile membranes, and (b) Velocity in the X direction at Y = 4.55 cm as a function of distance between the two textile membranes.

cross sections along the downcomer, and different superficial-gas velocities, the numerical model could correlate the experimental data in a similar way.[26] The surface jet has higher horizontal magnitudes close to the membrane compared to the rigid wall, as shown in Figure 12. This might be attributed to shear forces that weaken the intensity of the surface jet before impacting the rigid wall. It should be recalled that the direction of velocity vectors at the surface jet point in the opposite direction of the X-axis. Higher X-directed magnitudes provide lower Y-directed magnitudes in this region, as illustrated in Figure 13. Along the downcomer the magnitudes of horizontal and vertical velocity vectors are almost constant in X direction. Figures 12 and 13 also show that in proximity of outlet, however, higher horizontal and vertical flows happen close to the membrane. Figure 14 shows the effect of the distance between membranes on magnitude of horizontal flow. Increasing the distance between the membranes reduces horizontal flow at the surface jet and outlet zone, thereby decreasing the X-directed magnitudes of velocity vectors along the downcomer. The effect of bubble size on magnitude of horizontal flow is shown in Figure 15. Replacing the flexible porous tube with a rigid perforated one increases bubble size from 3 mm to 1.5 cm, and decreases substantially the corresponding horizontal velocity magnitudes. The new velocity profile, however, is still predictable with FVM. It suffices that one solves the code with the same boundary and initial conditions, but different surface jet velocity at the inlet, as shown in Figure 15.

Conclusions

Horizontal convective flow into the porous textile membrane would span a certain length of the membrane, aside from which convective flow changes to diffusive flow caused by hydrostatic-pressure difference across the membrane. The surface jet, which enters the downcomer zone, gains its intensity in the riser where the liquid is awash with rising bubbles. Uniform bubbles with high-specific surface area push higher volume of liquid upward in the riser and increase the intensity of the surface jet. The surface jet rams into the rigid wall of the contactor and produces two major streams. One is a wall jet that decelerates by 87% along the downcomer, and the other is a part of the surface jet that bounces back and clips the porous membrane. The latter was found to be responsible for the majority of the horizontal flow, mainly at the upper part of the membrane where hydrostatic pressure differences cease to be important. As a result, the effect of the horizontal flow recedes at downstream. Darcy's Law is the fundamental constitutive relationship used to understand the movement of fluid flow through the porous medium. The results of the numerical simulations for the case of U_{sg} = 0.023 cm/s were compared with that of the LIF visualization and LDV measurements. The model selected for the eddy viscosity was quite simple, and the results were in satisfactory agreement with the experiments.

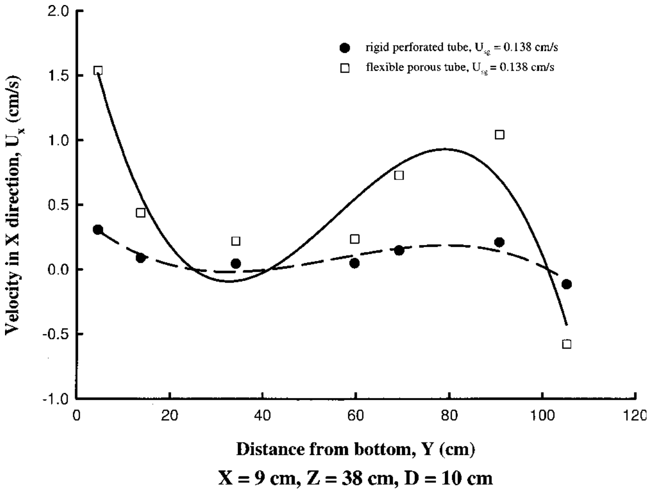

Figure 15. Velocity in the X direction as a function of distance from the bottom of vessel, using two different sparger types at.

The solid lines are obtained from the numerical model. The lines are predicted by the numerical model.

Notation

D = distance between membranes, m
d = thickness of membrane, m
H = liquid height, m
K = permeability coefficient, m^2
P = fluid pressure at membrane surface in downcomer zone, Ps
R^3 = 3-D space, m^3
S = surface, m^2
u = velocity, m/s
U = velocity, m/s
U_{sg} = superficial-gas velocity, m/s
W = distance between the membrane and the wall, m
X = rectangular coordinate, m
Y = rectangular coordinate, m
Z = rectangular coordinate, m

Greek notation

α = constant
β = constant
ε_g = gas holdup
μ = viscosity, kg/m.s
ν = kinematic viscosity of the fluid, m^2/s
ρ = density, kg/m^3
ψ = permittivity, s^{-1}
Ω = control volume, m^3

Acknowledgments

The authors are grateful to Imperial Oil, Ltd. and Natural Sciences and Engineering Research Council (NSERC) of Canada for financial support. B. Jajuee acknowledges support by the Western Engineering Scholarship. A Margaritis acknowledges support of this research through NSERC Discovery Grant No. A4388.

Literature Cited

1. Bumpus JA, Tien M, Wright D, Aust SD. Oxidation of persistent environmental pollutants by a white rot fungus. *Sci.* 1985;228:1434–1436.
2. Karamanev GD, Chavarie C, Samson R. Soil immobilization: new concept for biotreatment of soil contaminants. *Biotech Bioeng.* 1998; 57:471–476.
3. Petersen EE, Margaritis A. Hydrodynamic and mass transfer characteristics of three-phase gaslift bioreactor systems. *Crit Rev Biotech.* 2001;21(4):233–294.
4. Jianping W, Xiaoqiang J, Lei P, Changlin W, Guozhu M. Nitrifying treatment of wastewater from fertilizer production in a multiple airlift loop bioreactor. *Biochem Eng J.* 2005;25:33–37.
5. Bajpai P, Margaritis A. Studies on the flocculation characteristics of Kluyveromyces marxianus. *Biotech Bioeng.* 1986;28:283–287.
6. Margaritis A, Wallace JB. Novel bioreactor systems and their applications. *Biotech. (Nature Publ. Co.).* 1984;2:477–453.
7. Chisti YM, Halard B, Moo-Young M. Liquid circulation in airlift reactors. *Chem. Eng. Sci.* 1988;43:451–457.
8. Calvo EG, Letón P, Arranz MA. Prediction of gas hold up and liquid velocity in airlift loop reactors containing highly viscose Newtonian liquids. *Chem Eng Sci.* 1991;46:2951–2954.
9. Shamlou PA, Pollard DJ, Ison AP, Lilly MD. Gas holdup and liquid circulation rate in concentrichyphentube airlift bioreactors. *Chem Eng Sci.* 1994;49:303–312.
10. Godò Š, Klein J, Polakovič M, Báleš V. Periodical changes of input air flowrate- a possible way of improvement of oxygen transfer and liquid circulation in airlift bioreactors. *Chem Eng Sci.* 1999;54:4937–4943.
11. Wang S, Arimatsu Y, Koumatsu K, Furumoto K, Yoshimoto M, Fukumaga K, Nakao K. Gas holdup, liquid circulating velocity and mass transfer properties in a mini-scale loop airlift bubble column. *Chem Eng Sci.* 2003;58:3353–3360.
12. Blazej M, Kisa M, Markos J. Scale influence on the hydrodynamics of an internal loop airlift reactor. *Chem Eng and Proc.* 2004;43(12): 1519–1527.
13. Jajuee B, Margaritis A, Karamanev D, Bergougnou MA. Mass transfer characteristics of novel three-phase airlift contactor with a semipermeable membrane. *Chem Eng J.* 2006, in press.
14. Karamanev D, Margaritis A, Chong N. The application of ore immobilization to the bioleaching of refractory gold concentrate. *Int J Miner Process.* 2001;62(1-4):231–241.
15. Karel SF, Libicki SB, Robertson CR. The immobilization of whole cells: engineering principles. *Chem Eng Sci.* 1985;40:1321–1354.
16. Bajpai P, Margaritis A. Continuous hydrolysis of Fructans in Jerusalem artichoke extracts using immobilized non-viable cells of K. marxianus. *J Food Sci.* 1986;21(3):86–89.
17. Bajpai P, Margaritis A. Effect of temperature and pH on immobilized Zymomonas mobilis for continuous production of ethanol. *Biotech Bioeng.* 1986;28:824–828.
18. Margaritis A, Kilonzo, Production of ethanol using immobilized cell bioreactor systems. In:Nedovic B, Willaert R E, Application of cell immobilization biotechnology.Springer, Berlin; 2005:375–405.
19. Margaritis A, Bajpai P. Continuous ethanol production form Jerusalem artichoke tubers. Part II. Use of immobilized cells of Kluyveromyces marxianus. *Biotech Bioeng.* 1982;24(7):1483–1493.
20. Karimian SAM, Straatman AG. Discretization and parallel performance of an unstructured finite volume Navier-Stokes solver. *Int J Numer Meth Fluids.* 2006;52:591–615.
21. Smagorinsky J. General circulation experiment with the primitive equations, Part I: the basic experiment. *Monthly Weather Rev.* 1963;91:99–164.
22. Kaviany M.Principles of heat transfer in porous media. 2nd ed. New York, Springer-Verlag; 1995:17–25.
23. Godbole SP, Schumpe A, Shah YT. Hydrodynamics and mass transfer in non-Newtonian solution in a bubble column. *AIChE J.* 1984;30(2): 213–220.
24. Vasconcelos JMT, Rodrigues JML, Orvalho SCP, Alves SS, Mendes RL, Reis A. Effect of contaminants on mass transfer coefficients in bubble column and airlift contactors. *Chem Eng Sci.* 2003;58:1431–1440.
25. Gholamreza-Kashi S, Martinuzzi RJ, Baddour RE. Mean flow field of a non-buoyant rectangular surface jet. *ASCE J Hydr Eng.* 2006, in press.
26. Jajuee B.*Oxygen mass transfer and oil hydrocarbon biotreatment characteristics of a novel airlift immobilized bioreactor system.* The University of Western Ontario, London, Ontario, Canada; 2006:133-171. Ph.D. dissertation.

Manuscript received Dec. 18, 2005, and revision received July 8, 2006.